The structural basis for activation of voltage sensor domains in an ion channel TPC1

Alexander F. Kintzer†,[1], Evan M. Green†,[1], Pawel K. Dominik†,[1,2], Michael Bridges[3], Jean-Paul Armache[1], Dawid Deneka[2], Sangwoo S. Kim[2], Wayne Hubbell[3], Anthony A. Kossiakoff[2], Yifan Cheng*,[1,4], Robert M. Stroud*,[1]

[1]University of California, San Francisco, Department of Biochemistry and Biophysics

[2]University of Chicago, Department of Biochemistry and Molecular Biology

[3]University of California, Los Angeles, Jules Stein Eye Institute and Department of Chemistry and Biochemistry

[4]Howard Hughes Medical Institute

†These authors contributed equally to this work

Correspondence to Robert Stroud; stroud@msg.ucsf.edu and Yifan Cheng; YCheng@ucsf.edu

Abstract

Voltage sensing domains (VSDs) couple changes in transmembrane electrical potential to conformational changes that regulate ion conductance through a central channel. Positively charged amino acids inside each sensor cooperatively respond to changes in voltage. Our previous structure of a TPC1 channel captured the first example of a resting-state VSD in an intact ion channel. To generate an activated state VSD in the same channel we removed the luminal inhibitory Ca^{2+}-binding site (Ca_i^{2+}), that shifts voltage-dependent opening to more negative voltage and activation at 0 mV. Cryo-EM reveals two coexisting structures of the VSD, an intermediate state 1 that partially closes access to the cytoplasmic side, but remains occluded on the luminal side and an intermediate activated state 2 in which the cytoplasmic solvent access

to the gating charges closes, while luminal access partially opens. Activation can be thought of as moving a hydrophobic insulating region of the VSD from the external side, to an alternate grouping on the internal side. This effectively moves the gating charges from the inside potential to that of the outside. Activation also requires binding of Ca^{2+} to a cytoplasmic site (Ca_a^{2+}). An X-ray structure with Ca_a^{2+} removed and a near-atomic resolution cryo-EM structure with Ca_i^{2+} removed define how dramatic conformational changes in the cytoplasmic domains may communicate with the VSD during activation. Together four structures provide a basis for understanding the voltage dependent transition from resting to activated state, the tuning of VSD by thermodynamic stability, and this channel's requirement of cytoplasmic Ca^{2+}-ions for activation.

Introduction

Voltage sensing domains (VSDs) are four-helical bundle domains, termed S1-S4 that respond to changes in membrane potential by allowing 'gating' charges, generally positively charged arginine or occasionally lysine side chains in the fourth transmembrane helix S4 (charges referred to as R1-R5) to move relative to a charge-transfer center (CT) (1, 2) that contains counter charges in the surrounding helices S1-S3 and an aromatic residue (Y, F) that seals the VSD to solvent passage.

The number of gating charges in each VSD that move across the membrane from connection to the cytoplasmic side to the extracellular (or lumenal) side during activation is typically measured as 2-3 and up to 5 positive charges. The basis for structural and electrical changes in S4 that give rise to voltage-dependence is key to understanding the response of voltage-gated ion channels to changes in membrane potential.

In voltage-gated ion channels, the movement of S4 is connected via an S4-S5 linker helix on the cytoplasmic side to the pore helices S5-S6 of the ion channel, and also through Van der Waals hydrophobic contacts between S4 and the pore-forming domains. In excitable cells, activation of the VSD in response to membrane depolarization greatly increases the probability of channel opening(3, 4).

Several models have been proposed for voltage-dependent activation. The 'Sliding Helix'(5), 'Rotating helix'(6, 7), and 'Paddle'(8) models suggest that S4 moves substantially (vertically or in rotation) in the membrane to translate the gating charges across the membrane (Figure S1). In Sliding Helix and Rotating Helix models, the gating charges interact with counter anions or aqueous environments to avoid the energetic penalty of placing a charge in a hydrophobic environment. Lanthanide-based resonance energy transfer measurements suggest that gating charges do not move extensively during activation, but rather achieve alternating exposure to the internal and external milieu through conformational changes in the VSD helices S1-S4 (9). A 'ratchet' model also includes the possibility of multiple intermediate states of S4(10). Electrophysiology, electron paramagnetic resonance (EPR) spectroscopy, X-ray structures, disulfide crosslinking, and simulations support a combination of translation and rotation of S4 during activation (11–18). No structural information until now exists for voltage-gated channels captured in multiple activation states, precluding an atomic scale evaluation of the mechanism of voltage-dependent changes, or how they translate to channel activation.

Our previous crystal structure of wild-type *Arabidopsis thaliana* two-pore channel 1 ($AtTPC1_{WT}$) provided the first resting-closed state in an intact ion channel(19, 20), the electrophysiological state that forms under high lumenal 1 mM (>100µM) Ca^{2+}-ion concentration. Here we sought to determine structures for the activated-state of AtTPC1 that is

formed in low lumenal (<100µM) Ca^{2+}-ions by removing the inhibitory luminal Ca^{2+}-binding site in VSD2 (Ca_i^{2+}), while keeping the cytoplasmic activation site (Ca_a^{2+}) occupied with >300µM cytoplasmic Ca^{2+}-ions (21). Secondly, we wanted to determine the mechanism for the channel's requirement of cytoplasmic Ca^{2+}-ions for activation by removing the Ca_a^{2+} site.

TPCs are a family of ion channels that regulate ion conductance across endolysosomal membranes(21, 22, 23). Located in endosomes that endocytose from the plasma membrane, initially with ~1mM extracellular Ca^{2+} concentration, they regulate the conductance of Na^{+}- and/or Ca^{2+}-ions out of the endolysosome, intravesicular pH (24), trafficking (25), and membrane excitability (26). Cytoplasmic Ca^{2+}-ions (>300 µM) are required for any activation of AtTPC1 (27), whereas lumenal Ca^{2+}-ions (>100 µM) suppress voltage-dependent activation (20, 28). TPCs encode two pore-forming domains on a single chain with two non-equivalent VSDs (S1-S4, S7-S10) and pore helices (S5-S6, S11-S12). In AtTPC1 only VSD2s (S7-S10) respond to changes in voltage (20). Three arginines on S10 of each VSD2 (equivalent to S4 in the VSD of tetrameric ion channels) in AtTPC1 are required for voltage-dependent activation. A homo-dimer of two TPCs forms the central functional channel surrounded by four pore-forming domains. The dependence of AtTPC1 on external and internal Ca^{2+} offer the opportunity to visualize the resting state of a voltage sensing domain of an intact channel, and the activated state and to ask how voltage changes are detected and relayed.

Lumenal Ca^{2+}-ions suppress activation of AtTPC1 via binding to Ca_i^{2+} located in the active voltage sensor VSD2 with EC_{50} ~0.1mM. This previously enabled trapping of the resting-state VSD2 of wild-type AtTPC1 by including 1 mM Ca^{2+}-ions (19, 20). Replacement of the Ca^{2+}-chelating amino acids by mutagenesis (D240N, D454N, E528Q; termed $AtTPC1_{DDE}$) shifts voltage-dependent activation by -50 mV, such that the channel is open at 0 mV (20, 28) and

93 VSD2 in an activated conformation. Using $AtTPC1_{DDE}$ we sought to determine the structure of
94 an activated state of the same intact channel where we had previously determined a resting state.
95 Channel opening requires Ca^{2+}-ion binding to Ca_a^{2+} mediated by D376 of cytoplasmic EF-
96 hand domain helix 3-4 loop (EF3-EF4). Removal of cytoplasmic Ca^{2+}-ions or the mutation
97 D376A ($AtTPC1_{DA}$) yields permanently closed channels (29). The absolute requirement of the
98 Ca_a^{2+} site for voltage-dependent activation led us to hypothesize that channel activation depends
99 on communication between Ca_a^{2+} and VSD2 (21). Using the D376A mutation we sought to
100 determine how cytoplasmic Ca^{2+} evokes activation.
101
102 **Results and Discussion**
103 **Cryo-EM structures of $AtTPC1_{DDE}$**
104 As a basis for understanding the voltage-dependent activation mechanism and its modulation by
105 Ca^{2+}-ions, we determined the structure of $AtTPC1_{DDE}$ by cryo-EM (Figure 1a, Figure S2, S3, S4,
106 Table S1). We employed saposin A nanoparticles (30) to reconstitute $AtTPC1_{DDE}$ into a
107 membrane environment, and an antibody Fab made against AtTPC1 (CAT06/H12) (31) to
108 facilitate particle alignment (32) (Figures S5, S6, See Supplemental Discussion).
109 With a nominal resolution of 3.3 Å, the density map of $AtTPC1_{DDE}$ is of high quality
110 (Figure S4a), allowing additional *de-novo* interpretation of the AtTPC1 N-terminal domain
111 (NTD), the S1-S2 linker, EF3-EF4 with an intact Ca_a^{2+} site, the upper vestibule of the pore, and
112 the C-terminal domain (CTD). Three ions lie in the selectivity filter, consistent with previously
113 defined Ca^{2+}/Na^{+}-binding sites (19, 20, 33). Fourteen lipid molecules surround the channel in the
114 lumenal leaflet with two on the cytoplasmic side (Figure S7). S1-S6 are well defined and remain
115 stationary between all of the AtTPC1 structures. In $AtTPC1_{DDE}$, major rearrangements are

observed in the VSD2, the upper vestibule of pore, and EF3-EF4 on the cytoplasmic side, relative to $AtTPC1_{WT}$ (Figure 1b). The position of three residues known to be phosphorylated (S22, T26, and T29) are observed in previously unresolved portions of the NTD (Figure S4a, See Supplemental Discussion) (19).

The Fab binds to the EF1-EF2 loop, EF4, and S6 on the cytoplasmic side. The Fab binding affinity is the same with and without Ca^{2+} ions, in other molecular conditions tested (1 mM EGTA, 1 µM trans-NED19, 1 µM Nicotinic Acid Adenine Dinucleotide Phosphate), and in three different constructs ($AtTPC1_{WT}$, $AtTPC1_{DDE}$, $AtTPC1_{DA}$), indicating that the Fab binding does not distinguish between nor is likely to influence the activation state (Figure S5c-d). Most of the variable domain of the Fab is visible, allowing interpretation of the $AtTPC1_{DDE}$-Fab interface (Figure S6e-f). The constant domain of the Fab is flexible and not resolved to high resolution.

Activation of the voltage sensor

Lumenal Ca^{2+}-ions inhibit AtTPC1 channel activation half maximally at ~0.1 mM concentration(20) via binding to Ca_i^{2+} (21) between VSD2 (D454 in the S7-S8 loop, and E528 in S10), and the pore (D240). D454N, also named *fou2* (fatty acid oxygenation up-regulated 2) (28), abolishes inhibition by lumenal Ca^{2+}-ions, increasing channel open probability by shifting the voltage-dependent channel opening towards more hyperpolarizing potentials (28, 20). Ca^{2+}-ions do not inhibit $AtTPC1_{DDE}$ at 1 mM and up to 10 mM (33). Thus, the Ca_i^{2+} site is functionally abolished in $AtTPC1_{DDE}$ under cryo-EM conditions and thereby mimics the activated state under voltage and low lumenal Ca^{2+}-ion conditions (20, 33).

While the overall resolution of $AtTPC1_{DDE}$ is excellent, density for S7-S10 of VSD2 is significantly weaker indicating conformational heterogeneity. Focused classification identified two states of VSD2, each with an overall resolution of 3.7 Å, but with distinct and different conformations of the S7-S10 domain structure (state 1 and 2) (Table S1, Figure S3, See Methods). We therefore conclude that these two conformations represent different functional states of the $AtTPC1_{DDE}$ channel. They suggest a model for the voltage-activation of AtTPC1, and a mechanism for dependence on lumenal Ca^{2+}-ions.

To confirm that the structural rearrangements in VSD2 were not induced by saposin A we determined a ~7Å reconstruction of $AtTPC1_{WT}$ in both detergent and in saposin A. In these the overall channel architecture is comparable to the $AtTPC1_{WT}$ crystal structure (Figure S8).

The local resolution of VSD2 (S7-S10) ranges from 4-6 Å in both states, making it possible to model the intermediate active state of VSD2 based on the 2.8 Å X-ray structure of $AtTPC1_{WT}$ (Figure S4b, c, See Methods under Structure Determination and Refinement)(19). Atomic structures for states 1 and 2 were determined by real-space and B-factor refinement against the cryo-EM densities. Changes in solvent accessibility at the luminal and cytoplasmic boundaries of VSD2 were apparent from the comparison of these new structures of AtTPC1 and the previous resting-state. Taking the resting state structure of $AtTPC1_{WT}$ as a reference (PDBID 5DDQ; ref. (19)), transmembrane helices S7-S10 in state 1 rotate in a counterclockwise manner with respect to $AtTPC1_{WT}$ (Figure 2). The helices twist to partially close the cytoplasmic solvent access to the gating charges of VSD2 (Figure 3), while the lumenal face remains occluded. Among all helices of VSD2, the key arginine-rich S10 has the least movement, and R537 (R1) remains interacting with the CT (Y475), albeit the changes in S8 conformation place R1 on the opposite horizontal face of the CT as compared with $AtTPC1_{WT}$. S8 moves upward in the

membrane plane by nearly one helical turn, thus moving the CT into place to interact with R1 in similar manner to $AtTPC1_{WT}$. State 1 probably represents a resting-state structure present in low lumenal (<0.1 mM) Ca^{2+}-ion concentrations.

In state 2, VSD2 rotates ~20˚ clockwise in the plane of the membrane with respect to $AtTPC1_{WT}$ (Figure 2). Helices S7-S10 reorient dramatically leading to an opening of the lumenal face of VSD2 (Figure 3). Tilting of S10 and rotation of S8 around S10 moves the CT downward, placing R1 in an activated conformation. The cytoplasmic face is fully closed in state 2 while the lumenal side is partially open. VSD2 has effectively alternated solvent access, or electrical contact from the cytoplasmic to the lumenal side of the membrane.

Clockwise rotation was proposed to connect resting- and active-state conformations on the basis of comparing previous voltage-gated channel structures (13, 19, 34). During review of this manuscript, activated state structures of mouse TPC1 were determined (35). Comparing the activated-state mouse TPC1 to resting- and intermediate-state AtTPC1 supports the proposed role of VSD2 rotation during channel activation. The observation of clockwise rotation in multiple activated-state structures supports our conclusion that state 2 represents an intermediate-activated state of AtTPC1.

These two states of VSD2 in AtTPC1 are likely to represent structures that VSD2 adopts in low lumenal Ca^{2+} during activation. The overall movement of VSD2 during activation serves to dilate the lumenal face of VSD2, close off the cytoplasmic leaflet to solvent, and move the CT below a gating charge in the membrane. This would reconnect the positive gating charges from the potential of the cytoplasmic side to the potential of the lumenal side upon activation, mediated by tilt and twisting of S7, S8, S9 around S10. This is all that is necessary to transport the gating charge arginine residues from cytoplasmic electrical connection, to the external

potential. A hydrophobic sealed region between all four helices forms a thin outer insulating layer in the resting state, while in the activated state this becomes open to solvent and the bundle twists to form a hydrophobic insulating region closer to the cytoplasmic side.

Drug and Lipid Binding Sites

The high resolution map enabled refinement of a total of 14 lipids on the lumenal and 2 on the cytoplasmic leaflet of the membrane. The lumenal lipids are modeled as the 16-carbon containing palmitic acid, the predominant lipid length in soy polar lipids, whereas the cytoplasmic lipids are modeled as 18-carbon phosphatidic acid (PA). 12 lipids bind to the long axis of AtTPC1, occupying the binding site for Ned19 (Figure S7, ref. (19, 21)). Ned19 binding may disrupt these structured lipids, acting as a steric block to prevent S7 and pore movements during gating. One lipid binds to a buried site along the short axis, sandwiched in between the pore domains. Based on homology to Ca_v channels in this region and recent structures of bacterial Ca_v channels (Ca_vAb) bound to dihydropyridines (DHP) (amlodipine and nimodipine) and PPA (verapamil) inhibitors(36), the short axis in transmembrane segments S6 and S12 is a likely site for binding of Tetrandrine, a bis-benzylisoquinoline alkaloid isolated from the Chinese herb *Stephania tetrandra*(37) and approved medications of the DHP class of L-type Ca_v antagonists–all TPC channel blockers.

The lumenal PA lipids bind along the short axis in a pocket formed by S1 of VSD1, the S10-S11 linker, S11, and the S8-S9 linker of VSD2. The alkyl chains make Van der Waals interactions, whereas the phosphoglycerol headgroup makes hydrogen bonds to the backbone of W492 and to the sidechain of R498 and S8-S9 of VSD2. The S8-S9 linker moves 4Å inward in the $AtTPC1_{DDE}$ structure to form the PA binding site, which would not be intact in the

207 $AtTPC1_{WT}$ resting-state. Therefore, this lipid binding site is likely specific for $AtTPC1_{DDE}$.
208 Certain lipids may occupy this site during activation of AtTPC1. Polyunsaturated fatty acids
209 inhibit plant TPC1 activation, but the binding site has not been determined (38). In principle,
210 polyunsaturated fatty acids could mimic the observed site in the resting-state and prevent
211 activation.
212
213 **Charge transfer mechanism**
214 State 2 represents an intermediate activation state of VSD2 where the gating charge R1 is
215 transferred across the membrane (Figure 3). In this state, the CT moves downwards, R1 moves
216 slightly upwards, and overall the VSD2 bundle rotates by ~20˚ in the membrane plane with
217 respect to the adjacent pore domains. In this the voltage-sensing helix S10 pivots only 2-3˚
218 inward toward the pore. Importantly, the three observed states of the VSD thus far are not related
219 by rigid-body rotations. These changes in VSD2 make R1 more accessible to solvent on the
220 lumenal side while charges R2 and R3 are shielded from access to the cytoplasmic side; there is
221 a net transfer of charge from cytoplasmic side (in the resting state) to the outside (in the activated
222 state).
223
224 **Pore conformational changes**
225 High-resolution density for the pore defines the consequences of activation by removal of the
226 external Ca_i^{2+} site on VSD2 on the central channel (Figure 4a, b). As a consequence of the
227 rearrangement of VSD2 the upper vestibule and the upper selectivity filter of the channel open
228 along the ion permeation pathway (Figure 4c), while the lower gate remains closed (Figure 4d).
229 Full channel opening may be evoked by passage of ions or an additional energy barrier, because

electrophysiological studies show the channel is maximally open at 0 mV with removal of the Ca_i^{2+} site.

In the selectivity filter, three ions are observed (Figure 4e, f). Site 1 and 3 were occupied by Ca^{2+} mimetics, Yb^{3+} or Ba^{2+}, in $AtTPC1_{WT}$ structures (19, 20). Site 2 was seen to be occupied by Na^+ in the Na^+-selective chimera of AtTPC1(33). Since $AtTPC1_{DDE}$ contains 1 mM Ca^{2+} and the channel is Ca^{2+}-selective, these are probably hydrated Ca^{2+}-ions (See Supplemental Discussion). Sidechain interactions from the upper vestibule of S11-S12 exclusively coordinate site 1. The side chains of D606 move inward to coordinate site 1 with E605 (Figure 4g). E605-Ca^{2+} (5.5 Å) and D606-Ca^{2+} (4.6 Å) distances are consistent with the radius of a hydrated Ca^{2+} ion. There are readjustments throughout the channel suggesting that VSD2 activation by removal of the luminal Ca_i^{2+} site can indeed potentiate channel opening as observed by electrophysiology.

The observation of upper and lower selectivity filter and activation gate operating independently in our structures suggests a multi-step gating mechanism that resembles that proposed for TRPV1 channel activation (39). Activation of the VSDs could lead to opening of the selectivity filter and activation gate in two steps. First, the upper selectivity filter opens in response to rotational rearrangement and partial activation of the VSDs, then the lower selectivity filter and activation gate open when the VSD achieves maximal activation.

Cytoplasmic activation by Ca^{2+}-ions

Full voltage-dependent activation of AtTPC1 requires ~0.3 mM cytoplasmic Ca^{2+} evoked by Ca^{2+}-binding to the EF3-EF4 loop (20, 29). D376 in EF3 is critical; when substituted D376A in $AtTPC1_{DA}$ the channel remains closed and is no longer responsive to membrane potential (29). We determined the crystal structure of $AtTPC1_{DA}$ (Figure 5a, Table S2) to 3.5 Å resolution by

X-ray crystallography. When compared with the $AtTPC1_{WT}$ crystal structure, removing the activating cytoplasmic Ca_a^{2+} binding site leads to higher dynamic motion (B-factors) not only in the EF-hand and the CTD, but also in the VSDs and upper vestibule of the pore, showing that the activating cytoplasmic site may act through effects on the VSDs (See Supplemental Discussion).

$AtTPC1_{DA}$ is in a resting-state as expected. However, there is an overall effect of increasing the dynamical motion of VSD1, VSD2 and the pore (in the context of otherwise identical overall B-factors), showing that Ca_a^{2+} has an allosteric effect in stabilization that could impact voltage dependence (VSDs) and conductance (the pore). The regions of increased motion in $AtTPC1_{DA}$ correspond to the regions that undergo conformational change in $AtTPC1_{DDE}$, suggesting that there is a pathway for coupling cytoplasmic activation at Ca_a^{2+} to voltage dependence of activation in VSD2 and transmission to the pore.

The Ca_a^{2+} site in EF3 is fully formed in the cryo-EM structure of $AtTPC1_{DDE}$, whereas it was partially occupied in $AtTPC1_{WT}$ and was in a more extended conformation(19, 20) (Figure 5b). In $AtTPC1_{DDE}$, EF3 alone lies 7 Å closer to the transmembrane domain and rotates 20° to make close contacts with EF4 (Figure 5c). The Ca_a^{2+}chelating residues E374, D376, and D380 order the EF3-EF4 loop around the activating Ca_a^{2+} site (Figure 5c). Movement of EF3 leaves the EF1-EF2 Ca^{2+} site unaltered. Therefore, EF3 is capable of undergoing large-scale movements that change the structure of the cytoplasmic domains and their connection to VSD2, suggesting that activation on the cytoplasmic side can act reciprocally through VSD2.

The conformation of the cytoplasmic domains seen in $AtTPC1_{DDE}$, probably reflects the predominant structure in $AtTPC1_{WT}$ (rather than the crystal structure) because the conformation of EF3 is conserved in cryo-EM structures from several conditions; detergent and saposin A

nanoparticles of $AtTPC1_{WT}$, and $AtTPC1_{DDE}$, and when bound to either of two different Fab molecules (Figure S8c).

The CTD of AtTPC1 is indispensable for channel activation(40). Removal or truncation by 29 residues abolishes channel function. In the crystal structure of $AtTPC1_{WT}$, the CTD forms an intramolecular complex with the EF3 via salt-bridge interaction D376-R700, leading to the hypothesis that the EF3-CTD complex could undergo conformational changes upon activating cytoplasmic Ca^{2+}-binding (19). In the cryo-EM structures the CTD moves toward the membrane vertically by 13Å to accommodate the upward movement of EF3 upon forming the cytoplasmic activating Ca_a^{2+} site (Figure 5b). The salt-bridge (D376-R700) that previously linked the CTD to EF3 in $AtTPC1_{WT}$ breaks to allow D376 to chelate the Ca_a^{2+} site. This can explain why only substitution of D376 and not the other chelating residues abolishes Ca^{2+}-activation(29). In $AtTPC1_{DDE}$, the CTD now forms a hydrogen bond (E366-E694) with EF3 and hydrogen bonds (N697-I371) via the backbone (Figure 5d). Following the interaction with EF3, and a β-turn the CTD to folds back on itself to form a charged zippered interaction (R696-D691, R700-Q688, R707-E684) between the signal poly-R and poly-E motifs of the CTD (19). The poly-E motif connects directly to the pore gate (Figure 5e). The role of the CTD on channel activation may be to stabilize the EF3 helix in both apo- and Ca^{2+}-bound conformations to allow communication of EF3 movement to VSD2 and the pore gate. Upon removal of Ca^{2+}, the CTD could adopt an extended conformation to reform the salt-bridge interaction D376-R700 with EF3. Without the CTD, EF3 may not be able to reform the Ca_a^{2+} site and would become trapped in an inactive state.

To further investigate the conformation of EF3 in solution, we performed continuous wave electron paramagnetic resonance (CW-EPR) experiments using spin-labeled full-length

AtTPC1 lacking cysteines ($AtTPC1_{cysless}$; See Methods) in detergent micelles. Ten positions in the CTD, gate, and EF-hand domains were examined by spin-probe mobility and responsiveness to Ca^{2+}-ions. Labeling at a site on EF3 (R379) indicates a conformational shift to higher probe mobility as compared with EGTA, indicating that the probe changes environment in the presence of Ca^{2+}-ions (Figure S9). Mutation of the Ca_a^{2+} site but not the Ca^{2+}-site in EF1-EF2 abolishes the Ca^{2+}-dependent increase in probe mobility, suggesting that EF3/Ca_a^{2+} changes conformation upon increasing cytoplasmic Ca^{2+}-ion concentrations. The data suggest that the $AtTPC1_{WT}$ crystal structure likely represents an apo-state of EF3, whereas $AtTPC1_{DDE}$ represents a Ca^{2+}-bound conformation present along the pathway of activation.

Alternate Access Mechanism of Activation

As the electric potential changes across a membrane, functional voltage sensors find a new free energy minimum. Under hyperpolarizing conditions, the favorable electrostatic free energy component of positive gating charges' attraction to internal negative potential is balanced against a structural 'distortion' free energy cost. Depolarization therefore releases both of these components to populate a new overall equilibrium state that includes a component that regulates the open probability of the pore. Release of the electrostatic free energy is achieved by alternating access of the positively charged gating charges on S10 to solvent from the cytoplasmic side in the hyperpolarized resting state, to a state in which they are insulated from the cytoplasmic side, and become accessible to solvent from the lumenal side, without any necessity for vertical movement of the gating charges themselves. The structures of $AtTPC1_{WT}$ and $AtTPC1_{DDE}$ suggest that this 'alternating access' mechanism plays the key role. The

movement of the VSD2 helices S7, S8, S9 with respect to the gating charges on S10 achieve this (Figure 6).

Hence the potential gradient is focused across a thin hydrophobic region close to the lumenal (external) side in the resting-state, and alternately across one on the cytoplasmic side in the activated-state. Thus, the gating charges do not require any vertical movement across the bilayer as the electrically insulating region, which includes the CT and across which the voltage gradient is formed, moves from outside of the gating charges in the resting-state voltage sensor, to the cytoplasmic side of gating charges in the activated-state. Thus, the electric component of free energy is released.

The mechanism is unique versus most previously proposed models in that S7-S9, not only S10 that is closest to the pore, are crucial during voltage-activation to move gating charges from the electric potential on one side of the membrane to the potential of the other side without any necessary vertical translation of S10. Even after this major driving effect, gating charge side chains will also readjust in context of their different environments and some vertical movement may find more favorable energetics in the shallow energy gradient around them.

There is a teleologically favorable aspect to this alternate access mechanism in that it does not need to remove any hydrophobic residues out of the bilayer as would be required of a model involving large vertical movement of S10. It also does not need to rebuild the hydrophobic interface between S10 of the VSD and the walls of the pore with which it forms the primary contact that may be important in changes that alter open probability of the channel. Simulations of VSDs that assume a linear gradient of electric potential across the bilayer that changes only in slope on depolarization, but not position of start and end points across the VSD may not represent the true physiological state.

The Gibbs free energy change on moving one charge across a transmembrane potential difference of -70 mV is -1.6 kcal/mole. The measured gating charge transfer for activation of AtTPC1 is 3.9 charges(20) or -6.3 kcal/mole in free energy difference. Ca^{2+} that effectively stabilizes the resting-state. The EC_{50} for the Ca_i^{2+} site is ~0.1 mM. Therefore, assuming a K_d ~0.1 mM, the free energy released by removing each Ca_i^{2+} site is ~5.6 kcal/mole per site (or ~11.2 kcal/mole per AtTPC1 channel). It is not unreasonable that this difference, in releasing the restraint at Ca_i^{2+}, could allow the VSD to reach its active state that would normally be evoked by depolarizing the transmembrane potential at low Ca^{2+}. The fact that we observe intermediate states of TPC1 upon removing Ca_i^{2+} rather than the fully activated state suggests that the membrane voltage may contribute additional energy to maximize activation of VSD2 and channel open probability.

The mechanism suggested for AtTPC1 voltage dependent activation is the first time that atomic structures have been determined for intermediates on transition from resting-state to activated-state in an intact voltage-dependent channel. The structures also capture large-scale rotation of VSDs that could play a role in activation. It could be a general way in which gating charge can move energetically downhill in response to a change in voltage, without the energetic cost of removing any hydrophobic lipophilic regions out of the membrane.

Acknowledgements. We thank J. Finer-Moore for aiding with manual building, refinement, and critical reading of the manuscript. We thank A. Brilot, K. Verba, E. Palovcak, and D. Asarnow for help with data processing and refinement, R. Wang for help using Rosetta, D. Bulkley and M. Braunfeld at UCSF, and Z. Yu and his colleagues at the HHMI Janelia Cryo-EM Facility for aiding with data collection, and Ali Punjani for a pre-release version of cryoSPARC v2. This

366 work was supported by NIH grant GM24485 (to R.M.S), Postdoctoral Independent Research
367 Grant (to A.F.K) from the University of California, San Francisco Program for Breakthrough
368 Biomedical Research, which is partially funded by the Sandler Foundation, NIH grants
369 R01GM098672, S10OD020054, and S10OD021741 (to Y.C.), NIH grants GM117372 and
370 GM087519 (to A.A.K), and NIH grants R01EY05216 and P30EY00331, and the Jules Stein
371 Professor Endowment, and the Bruce Ford and Anne Smith Bundy Foundation (to W.H.). E.M.G
372 was supported by the National Science Foundation Graduate Research Fellowship NSF 1144247.
373 Beamline 8.3.1 at the Advanced Light Source is operated by the University of California Office
374 of the President, Multicampus Research Programs and Initiatives grant MR-15-328599. The
375 Berkeley Center for Structural Biology is supported in part by NIH, NIGMS, and HHMI. The
376 Advanced Light Source is supported Contract No. DE-AC02-05CH11231. Stanford Synchrotron
377 Radiation Lightsource Contract No. DE-AC02-76SF00515. The SSRL Structural Molecular
378 Biology Program is supported by the DOE, and P41GM103393. Chimera was supported by
379 NIGMS P41-GM103311.

380 **Author Contributions.** A.F.K. conceived and designed the project with assistance of R.M.S.
381 A.F.K. and P.K.D. purified TPC1. A.F.K. performed crystallization and structure determination
382 experiments, refined crystal and cryo-EM structures, and optimized saposin A reconstitution;
383 E.M.G. collected and processed cryo-EM data with J-P.A. and Y.C.; P.K.D. reconstituted TPC1
384 into nanodiscs and generated Fabs with D.D., S.S.K., and A.A.K.; M.B. collected EPR data with
385 W.H.; A.F.K., E.M.G., Y.C., and R.M.S. wrote the manuscript. All authors contributed to
386 manuscript preparation.

387 **References**

388 1. Hille B (2001) *Ion Channels of Excitable Membranes, Third Edition* (Sinauer Associates,
389 Sunderland, Mass). 3rd Edition edition.

2. Tao X, Lee A, Limapichat W, Dougherty DA, MacKinnon R (2010) A Gating Charge Transfer Center in Voltage Sensors. *Science* 328(5974):67–73.

3. Aggarwal SK, MacKinnon R (1996) Contribution of the S4 Segment to Gating Charge in the Shaker K+ Channel. *Neuron* 16(6):1169–1177.

4. Seoh S-A, Sigg D, Papazian DM, Bezanilla F (1996) Voltage-Sensing Residues in the S2 and S4 Segments of the Shaker K+ Channel. *Neuron* 16(6):1159–1167.

5. Catterall WA (1986) Molecular Properties of Voltage-Sensitive Sodium Channels. *Annu Rev Biochem* 55(1):953–985.

6. Guy HR, Seetharamulu P (1986) Molecular model of the action potential sodium channel. *Proc Natl Acad Sci U S A* 83(2):508–512.

7. Gandhi CS, Isacoff EY (2002) Molecular Models of Voltage Sensing. *J Gen Physiol* 120(4):455–463.

8. Jiang Y, Ruta V, Chen J, Lee A, MacKinnon R (2003) The principle of gating charge movement in a voltage-dependent K+ channel. *Nature* 423(6935):42–48.

9. Bezanilla F (2000) The Voltage Sensor in Voltage-Dependent Ion Channels. *Physiol Rev* 80(2):555–592.

10. Bezanilla F, Perozo E, Stefani E (1994) Gating of Shaker K+ channels: II. The components of gating currents and a model of channel activation. *Biophys J* 66(4):1011–1021.

11. Lu Z, Klem AM, Ramu Y (2002) Coupling between Voltage Sensors and Activation Gate in Voltage-gated K+ Channels. *J Gen Physiol* 120(5):663–676.

12. Perozo E, Cortes DM, Cuello LG (1998) Three-dimensional architecture and gating mechanism of a K+ channel studied by EPR spectroscopy. *Nat Struct Mol Biol* 5(6):459–469.

13. Payandeh J, Scheuer T, Zheng N, Catterall WA (2011) The crystal structure of a voltage-gated sodium channel. *Nature* 475(7356):353–358.

14. Li Q, et al. (2014) Structural mechanism of voltage-dependent gating in an isolated voltage-sensing domain. *Nat Struct Mol Biol* 21(3):244–252.

15. Zhang X, et al. (2012) Crystal structure of an orthologue of the NaChBac voltage-gated sodium channel. *Nature* 486(7401):130–134.

16. Long SB, Campbell EB, Mackinnon R (2005) Crystal structure of a mammalian voltage-dependent Shaker family K+ channel. *Science* 309(5736):897–903.

17. Yarov-Yarovoy V, Baker D, Catterall WA (2006) Voltage sensor conformations in the open and closed states in rosetta structural models of K+ channels. *Proc Natl Acad Sci* 103(19):7292–7297.

18. Yarov-Yarovoy V, et al. (2012) Structural basis for gating charge movement in the voltage sensor of a sodium channel. *Proc Natl Acad Sci* 109(2):E93–E102.

19. Kintzer AF, Stroud RM (2016) Structure, inhibition and regulation of two-pore channel TPC1 from Arabidopsis thaliana. *Nature* 531(7593):258–264.

20. Guo J, et al. (2016) Structure of the voltage-gated two-pore channel TPC1 from Arabidopsis thaliana. *Nature* 531(7593):196–201.

21. Kintzer AF, Stroud RM (2018) On the structure and mechanism of two-pore channels. *FEBS J* 285(2):233–243.

22. Hedrich R, Marten I (2011) TPC1 – SV Channels Gain Shape. *Mol Plant* 4(3):428–441.

23. Patel S (2015) Function and dysfunction of two-pore channels. *Sci Signal* 8(384):re7–re7.

24. Wang X, et al. (2012) TPC proteins are phosphoinositide- activated sodium-selective ion channels in endosomes and lysosomes. *Cell* 151(2):372–383.

25. Sakurai Y, et al. (2015) Two-pore channels control Ebola virus host cell entry and are drug targets for disease treatment. *Science* 347(6225):995–998.

26. Cang C, Bekele B, Ren D (2014) The voltage-gated sodium channel TPC1 confers endolysosomal excitability. *Nat Chem Biol* 10(6):463–469.

27. Hedrich R, Neher E (1987) Cytoplasmic calcium regulates voltage-dependent ion channels in plant vacuoles. *Nature* 329(6142):833–836.

28. Beyhl D, et al. (2009) The fou2 mutation in the major vacuolar cation channel TPC1 confers tolerance to inhibitory luminal calcium. *Plant J* 58(5):715–723.

29. Schulze C, Sticht H, Meyerhoff P, Dietrich P (2011) Differential contribution of EF-hands to the Ca2+-dependent activation in the plant two-pore channel TPC1. *Plant J* 68(3):424–432.

30. Frauenfeld J, et al. (2016) A saposin-lipoprotein nanoparticle system for membrane proteins. *Nat Methods* 13(4):345–351.

31. Dominik PK, et al. (2016) Conformational Chaperones for Structural Studies of Membrane Proteins Using Antibody Phage Display with Nanodiscs. *Structure* 24(2):300–309.

32. Wu S, et al. (2012) Fabs enable single particle cryoEM studies of small proteins. *Struct Lond Engl 1993* 20(4):582–592.

33. Guo J, Zeng W, Jiang Y (2017) Tuning the ion selectivity of two-pore channels. *Proc Natl Acad Sci* 114(5):1009–1014.

34. Catterall WA, Wisedchaisri G, Zheng N (2017) The Chemical Basis for Electrical Signaling. *Nat Chem Biol* 13(5):455–463.

35. She J, et al. (2018) Structural insights into the voltage and phospholipid activation of the mammalian TPC1 channel. *Nature* 556(7699):130–134.

36. Tang L, et al. (2016) Structural basis for inhibition of a voltage-gated Ca2+ channel by Ca2+ antagonist drugs. *Nature* 537(7618):117–121.

37. Zhang L, et al. (2009) Ionic liquid-based ultrasound-assisted extraction of fangchinoline and tetrandrine from Stephaniae tetrandrae. *J Sep Sci* 32(20):3550–3554.

38. Gutla PVK, Boccaccio A, De Angeli A, Gambale F, Carpaneto A (2012) Modulation of plant TPC channels by polyunsaturated fatty acids. *J Exp Bot* 63(17):6187–6197.

39. Cao E, Liao M, Cheng Y, Julius D (2013) TRPV1 structures in distinct conformations reveal activation mechanisms. *Nature* 504(7478):113–118.

40. Larisch N, et al. (2016) The function of the two-pore channel TPC1 depends on dimerization of its carboxy-terminal helix. *Cell Mol Life Sci* 73(13):2565–2581.

41. Alvarez FJD, Orelle C, Davidson AL (2010) Functional Reconstitution of an ABC Transporter in Nanodiscs for Use in Electron Paramagnetic Resonance Spectroscopy. *J Am Chem Soc* 132(28):9513–9515.

42. Borowska MT, Dominik PK, Anghel SA, Kossiakoff AA, Keenan RJ (2015) A YidC-like Protein in the Archaeal Plasma Membrane. *Struct Lond Engl 1993* 23(9):1715–1724.

43. Bailey LJ, et al. (2017) Locking the Elbow: Improved Antibody Fab Fragments as Chaperones for Structure Determination. *J Mol Biol*. doi:10.1016/j.jmb.2017.12.012.

44. Kabat EA, Wu TT, Foeller C, Perry HM, Gottesman KS (1992) *Sequences of Proteins of Immunological Interest* (DIANE Publishing).

45. Ritchie TK, et al. (2009) Chapter Eleven - Reconstitution of Membrane Proteins in Phospholipid Bilayer Nanodiscs. *Methods in Enzymology*, Liposomes, Part F., ed Düzgünes N (Academic Press), pp 211–231.

46. Kawate T, Gouaux E (2006) Fluorescence-detection size-exclusion chromatography for precrystallization screening of integral membrane proteins. *Struct Lond Engl 1993* 14(4):673–681.

47. Miller KR, et al. (2012) T Cell Receptor-Like Recognition of Tumor In Vivo by Synthetic Antibody Fragment. *PLOS ONE* 7(8):e43746.

48. Dominik PK, Kossiakoff AA (2015) Phage display selections for affinity reagents to membrane proteins in nanodiscs. *Methods Enzymol* 557:219–245.

49. Fellouse FA, et al. (2007) High-throughput generation of synthetic antibodies from highly functional minimalist phage-displayed libraries. *J Mol Biol* 373(4):924–940.

50. Zhang K (2016) Gctf: Real-time CTF determination and correction. *J Struct Biol* 193(1):1–12.

51. Scheres SHW (2012) RELION: implementation of a Bayesian approach to cryo-EM structure determination. *J Struct Biol* 180(3):519–530.

52. Zheng SQ, et al. (2017) MotionCor2: anisotropic correction of beam-induced motion for improved cryo-electron microscopy. *Nat Methods* 14(4):331.

53. Punjani A, Rubinstein JL, Fleet DJ, Brubaker MA (2017) cryoSPARC: algorithms for rapid unsupervised cryo-EM structure determination. *Nat Methods* 14(3):290–296.

54. Wang RY-R, et al. (2016) Automated structure refinement of macromolecular assemblies from cryo-EM maps using Rosetta. *eLife* 5:e17219.

55. Emsley P, Cowtan K (2004) Coot: model-building tools for molecular graphics. *Acta Crystallogr D Biol Crystallogr* 60(Pt 12 Pt 1):2126–2132.

56. Adams PD, et al. (2010) PHENIX: a comprehensive Python-based system for macromolecular structure solution. *Acta Crystallogr D Biol Crystallogr* 66(2):213–221.

57. Pettersen EF, et al. (2004) UCSF Chimera--a visualization system for exploratory research and analysis. *J Comput Chem* 25(13):1605–1612.

58. Davis IW, Murray LW, Richardson JS, Richardson DC (2004) MOLPROBITY: structure validation and all-atom contact analysis for nucleic acids and their complexes. *Nucleic Acids Res* 32(Web Server issue):W615-619.

59. Barad BA, et al. (2015) EMRinger: side chain-directed model and map validation for 3D cryo-electron microscopy. *Nat Methods* 12(10):943–946.

60. Gourdon P, et al. (2011) HiLiDe—Systematic Approach to Membrane Protein Crystallization in Lipid and Detergent. *Cryst Growth Des* 11(6):2098–2106.

61. Winn MD, et al. (2011) Overview of the CCP4 suite and current developments. *Acta Crystallogr D Biol Crystallogr* 67(4):235–242.

513 62. Strong M, et al. (2006) Toward the structural genomics of complexes: Crystal structure of a
514 PE/PPE protein complex from Mycobacterium tuberculosis. *Proc Natl Acad Sci*
515 103(21):8060–8065.

516 63. Kabsch W (1993) Automatic processing of rotation diffraction data from crystals of initially
517 unknown symmetry and cell constants. *J Appl Crystallogr* 26(6):795–800.

518 64. McCoy AJ, et al. (2007) Phaser crystallographic software. *J Appl Crystallogr* 40(4):658–674.

519

520

521 **Figures**

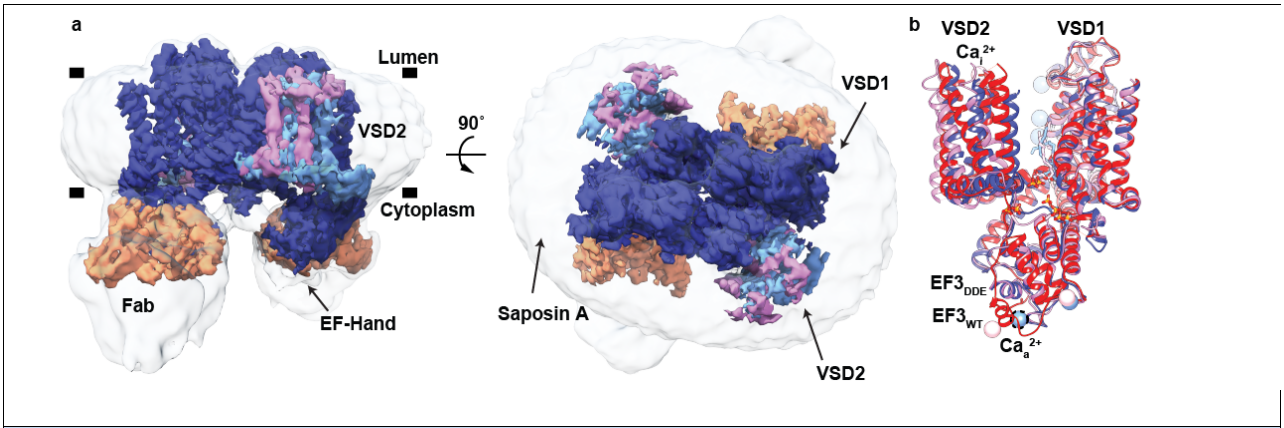

Figure 1. Cryo-EM Structure of the AtTPC1$_{DDE}$-saposin A-Fab complex. a, Side (left) and top-down (right) views of cryo-EM density. The composite map is colored to highlight high-resolution features of TPC1 (blue, EMDB 8957), VSD2 in state 1 (cyan, EMDB 8958) and state 2 (pink, EMDB 8960), and the Fab variable domains (orange, EMDB 8956). Unsharpened density is shown at low contour (transparent gray). Membrane boundaries (black bars) defined by the nanodisc are marked. b, Overlay of AtTPC1$_{WT}$ (red, PDBID 5DQQ), state 1 (blue), and state 2 (pink). Ca_i^{2+} and Ca_a^{2+} denote sites of lumenal inhibition and cytoplasmic activation by Ca^{2+}-ions. Dash lines around Ca_a^{2+} indicate hypothetical position in cryo-EM structure. Ca^{2+}-ions shown as colored balls.

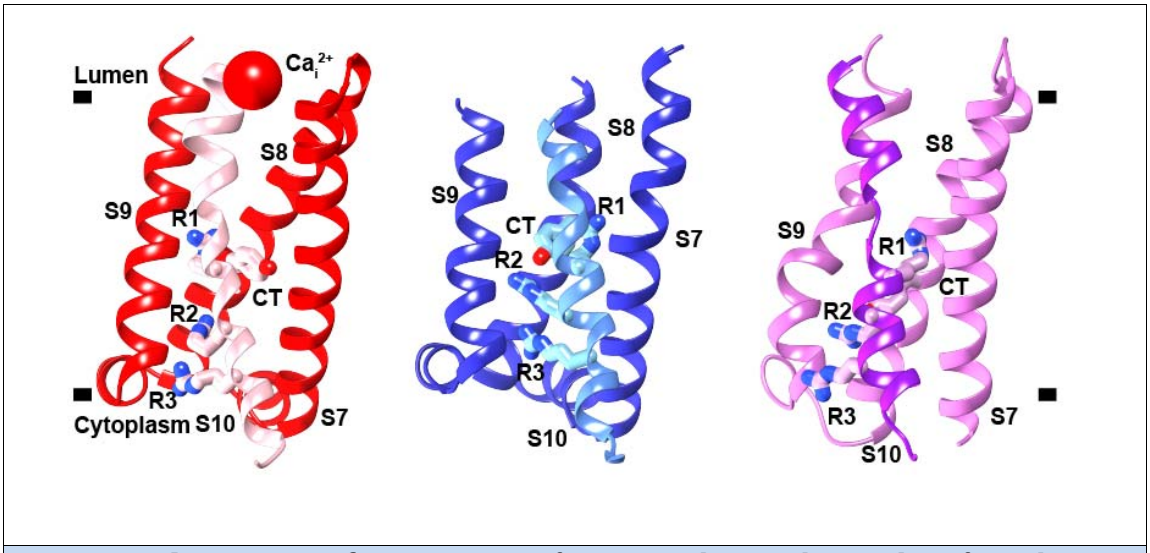

Figure 2. Three States of VSD2. View of VSD2 in the membrane plane from the center of the channel looking outward, that illustrates the rotation and twisting of VSD2 helices S7, S8, S9, and S10. Connections to the pore domains omitted for clarity. S10 is highlighted in each state with a different color than the other helices. Gating charges R1-R3 (R537, R540, R543), and CT residue Y475 are shown. Left: resting-state $AtTPC1_{WT}$ (red, PDBID 5DQQ), Center: $AtTPC1_{DDE}$ state 1 (blue), and Right: $AtTPC1_{DDE}$ state 2 (pink).

522

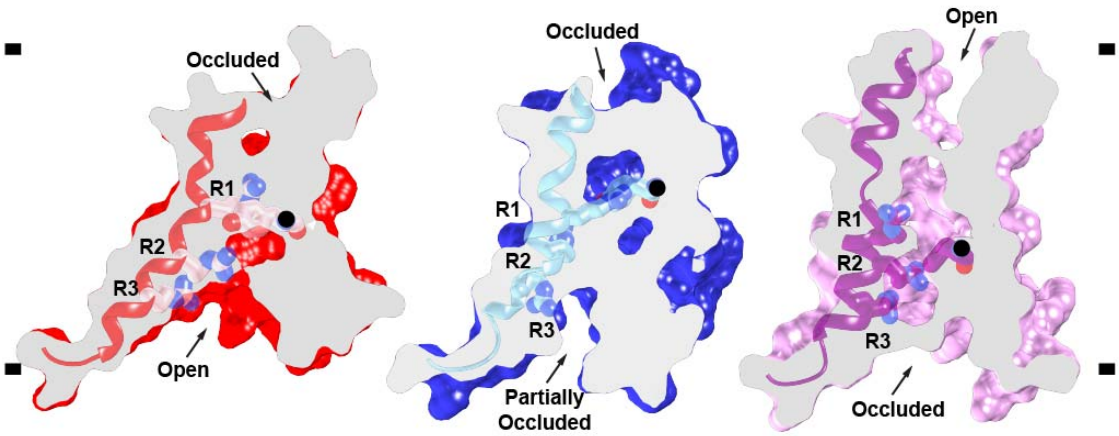

Figure 3. Activation of the Voltage-sensor. Side views of a common slice perpendicular to the membrane surface of VSD2 in $AtTPC1_{WT}$ resting-state (red, PDBID 5DQQ) and $AtTPC1_{DDE}$ state 1 (blue) and state 2 (pink). S10 shown with gating charges R1-R3. The CT C□ position (black ball) is marked. Based on a structural alignment with respect to the pore helices S6-S7 of each structure.

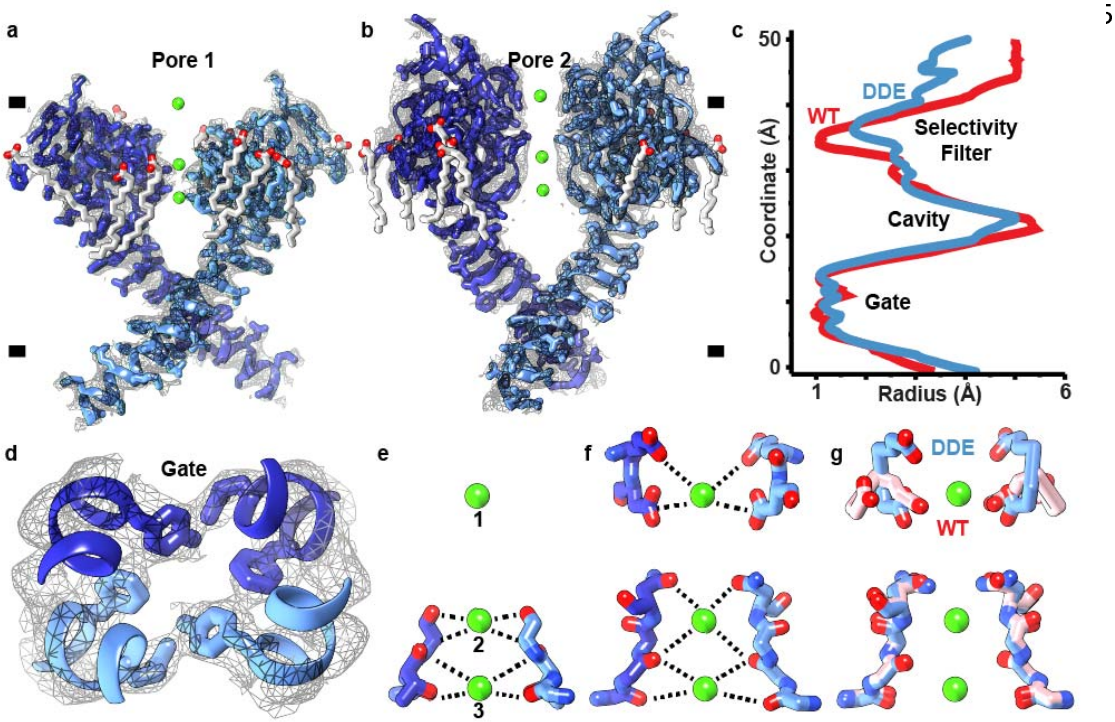

Figure 4. Ion Permeation Pathway. a, b, Orthogonal side views through pore helices (a) S5-S6 (pore 1) and (b) S11-S12 (pore 2) of the channel homo-dimer overlaid with high-resolution cryo-EM density (gray mesh). c, HOLE plot of pore radii along central channel coordinate of $AtTPC1_{DDE}$ (red) and $AtTPC1_{WT}$ (blue). d, Top down view through central pore. Gate residues Y305, L673, and F676 are shown. e-g, Side views through the selectivity filter in (e) pore 1, (f) pore 2, and (g) an overlay of pore 2 of $AtTPC1_{DDE}$ (blue) and $AtTPC1_{WT}$ (pink). Upper E605, D606 and lower S265, T263, T264, V628, M629, N631 selectivity filter residues are shown. Density for lipids (See Figure S7) and ions omitted for clarity.

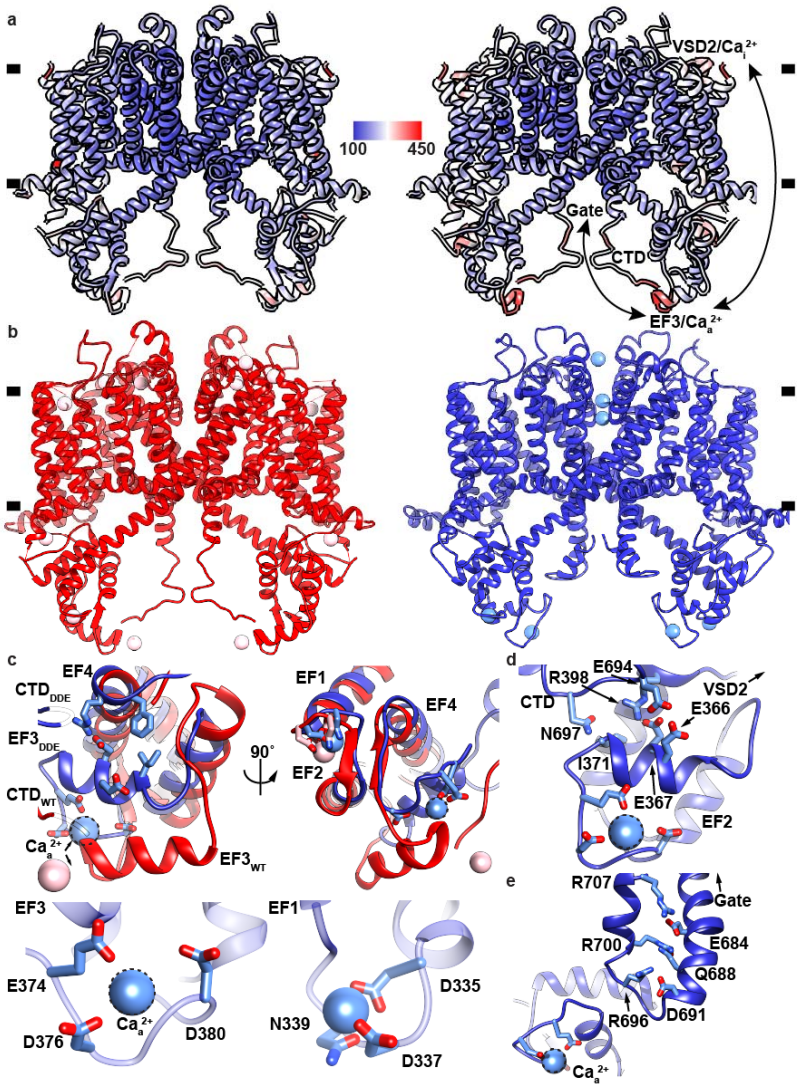

Figure 5. Dynamics of Cytoplasmic Domains. a, Overlay of (left) AtTPC1$_{WT}$ and (right) AtTPC1$_{DA}$ crystal structures colored by B-factor value (100-450 Å^2) (See Methods and Supplemental Discussion). b, Sideviews of AtTPC1$_{WT}$ (red) and AtTPC1$_{DDE}$ (blue). c, Views from (top left) side and (top right) bottom of EF3 for overlaid AtTPC1$_{DDE}$ (blue) and AtTPC1$_{WT}$ crystal structures (red, PDBID 5DQQ). CTD interactions omitted for clarity. Bottom panels show Ca^{2+}-ion binding sites in (bottom right) EF1-EF2 and (bottom left) EF3-EF4. d, View of EF3-CTD and EF3-EF4 interactions and connection to VSD2. e, Structure of the CTD in AtTPC1$_{DDE}$ and a possible coupling pathway to the pore gate and Ca_a^{2+}. Dash lines indicate the hypothetical Ca_a^{2+} ion position.

526

527

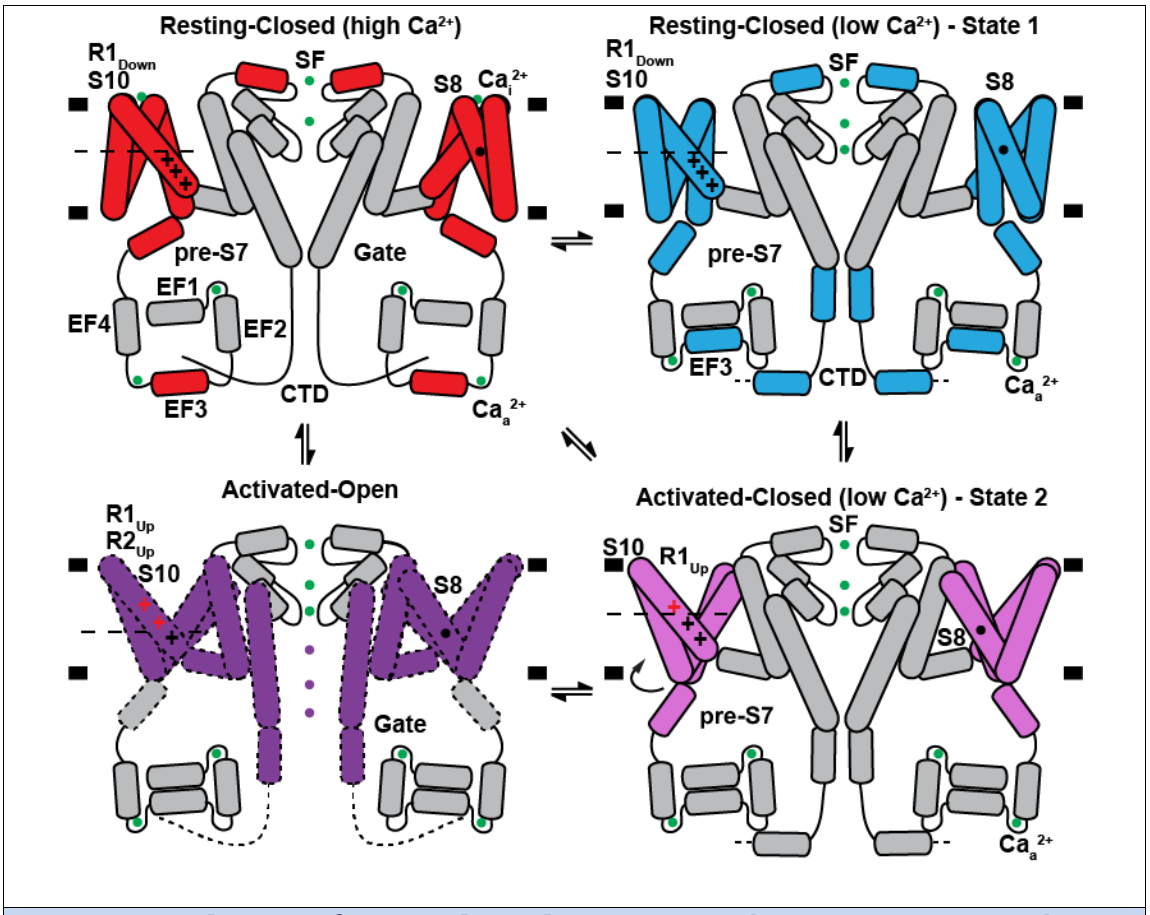

Figure 6. Mechanism of TPC1 Channel Activation. Schematic summarizing the conformations of VSD2, EF3, CTD, and selectivity filter (SF) observed in crystal and cryo-EM structures under high and low effective lumenal Ca^{2+}-ion concentrations. A potential model for coupling between lumenal inhibition Ca_i^{2+}, cytoplasmic activation Ca_a^{2+}, voltage-sensing, and channel gating is shown. Helices and ions that move between the $AtTPC1_{WT}$ resting-state (red), $AtTPC1_{DDE}$ state 1 (cyan), $AtTPC1_{DDE}$ state 2 (pink), and hypothetical activated-open state (purple) are colored. Ca^{2+}-ions are shown as green balls. Gating charges that change position with respect to the CT (dashed line) between states are colored red.

Methods

Protein Production

AtTPC1. X-ray and cryo-EM trials used AtTPC1 with deletion of residues 2-11(19). Antibody generation employed full-length AtTPC1. AtTPC1 constructs were expressed and purified by nickel affinity chromatography (NiNTA), thrombin cleavage, and size exclusion, as described previously(19). For reconstitution into saposin A lipoprotein nanoparticles and MSP nanodiscs, the size exclusion step was omitted after NiNTA, but performed after reconstitution. To introduce single cysteine labels for CW-EPR, a cysteine-less variant of AtTPC1, $AtTPC1_{cysless}$, was constructed to replace all native cysteines with serines (C93S, C101S, C159S, C347S, C392S, C574S, C577S, C580S, C687S, C728S). Cysteine substitutions for EPR spectroscopy were purified in the presence of 1mM TCEP during solubilization and binding to Nickel beads, but then removed during wash and elution steps to prevent interference with MTSL-labeling. $AtTPC1_{cysless}$ has identical biochemical behavior to wild-type AtTPC1.

Saposin A. Human saposin A (plasmid was a kind gift from J. Frauenfeld and P. Nordlund) was expressed and purified from *E. coli* Rosetta-gami 2(DE3) cells essentially as described(30). Several colonies from transformed cells were used to inoculate overnight 300 mL LB cultures containing 25 µg/mL chloramphenicol, 10 µg/mL tetracycline, and 15 µg/mL kanamycin at 37 ˚C. Overnight cultures were used to seed 6 L of Terrific Broth, grown to an absorbance value at 600 nm of 1. The temperature was adjusted to 20 ˚C 30 minutes prior to induction by 0.7 mM IPTG for 15 hours at 20 ˚C. Cells were harvested by centrifugation at 4,000x g for 10 minutes and resuspended in 200 mL 50 mM tris pH 7.4, 150 mM NaCl (Lysis Buffer) and frozen at -80 ˚C before further use. Bacterial pellets were lysed in the presence of 1 mM phenylmethylsulfonyl

fluoride (PMSF) by sonication for 5 minutes, then clarified by centrifugation at 26,000x g for 20 minutes. The supernatant was then incubated at 70 ˚C for 10 minutes followed by centrifugation at 26,000x g for 20 minutes to remove contaminant proteins. Imidazole pH 7.4 was then added to 20 mM and passed through two HisTrap FF crude 5mL columns equilibrated in Lysis Buffer with 20 mM Imidazole pH 7.4 using a peristaltic pump. Following 50 mL washes with Lysis Buffer with 20 mM Imidazole pH 7.4 and Lysis Buffer with 35 mM Imidazole pH 7.4, pure human saposin A was eluted in 25 mL Lysis Buffer with 400 mM Imidazole pH 7.4 in 1.5 mL fractions. Fractions containing human saposin A were dialyzed against 1 L of Lysis Buffer with 4 mg of Tobacco Etch Virus (TEV) protease. The following morning an additional 2 mg of TEV was added with an exchange of the dialysis buffer and dialyzed at room temperature for 3 hours. Uncleaved saposin A and free TEV were removed by passing the protein through a single HisTrap FF crude 5 mL column equilibrated in Lysis Buffer with 20 mM Imidazole pH 7.4 and washed with 30 mL of Lysis Buffer with 20 mM Imidazole pH 7.4. The flow-through and wash fractions were pooled and concentrated in 5 kDa molecular weight cutoff concentrators and serially injected in 20 mg aliquots over TSKgel G3000SW 7 mm x 60 cm or Superdex S200 10/300 columns equilibrated in Lysis Buffer with 1 mM $CaCl_2$. High and low molecular weight peaks were observed during size exclusion. The low molecular weight, most consistent with the size of the saposin A monomers and dimers, was concentrated to 2 mg/mL for use in reconstitution of AtTPC1 and frozen at -80 ˚C. Final yields of human saposin A were 5-10 milligrams of human saposin A per liter of culture.

Membrane scaffold protein. Plasmid harboring His-tagged E3D1 variant of membrane scaffold protein (MSP) of the nanodiscs was obtained from Addgene (#20066). MSP was expressed, purified and cleaved with TEV protease as described(41) with minor modifications. Colonies of

transformed BL21 (DE3) Gold cells (Stratagene) were used to inoculate overnight 30 mL LB cultures containing 30 µg/mL kanamycin. Overnight cultures were used to inoculate 2 L of Terrific Broth, grown at 37 ˚C until OD_{600} of 1.3 and then induced with 1 mM IPTG for 3 hrs. Cultures were harvested by centrifugation at 4,000x g for 10 minutes, resuspended in 50 mM Tris pH 8.0, 300 mM NaCl (MSP Lysis Buffer) supplemented with 1% Triton X-100, protease inhibitor tablet and 1 mM PMSF. Microtip sonicator (Branson) was used to lyse the cells for 3 cycles at 1s on, 1 off and at 60% amplitude for 3 minutes each. For each 1L culture 1 mL of NiNTA resin equilibrated with MSP Lysis Buffer was used in batch-binding for 1 hour at 4 ˚C. Resin was then washed with MSP Lysis Buffer supplemented with: 1) 1% Triton X-100 - 10 column volumes (CVs), 2) 50 mM sodium cholate, 20 mM imidazole – 5 CVs, 3) 50 mM imidazole – 7 CVs. MSP was eluted with 4 CVs of MSP Lysis Buffer supplemented with 400 mM imidazole. TEV cleavage was performed overnight in dialysis against 4 L of 50 mM Hepes pH 7.5 and 200 mM NaCl. Uncut protein was removed with subtractive step on NiNTA resin and cleaved MSP was concentrated to 5 mg/mL using Millipore concentrators with 10 kDa molecular weight cutoff and frozen in aliquots at -80 ˚C. Typical yield of MSP E3D1 from 1 L culture was 15 mg.

Antibodies. Monoclonal antibodies were expressed and purified from hybridoma culture supernatants using standard methods in the Monoclonal Antibody Core Facility at OHSU (Dan Cawley). 4B8 Fab fragment was generated by papain digestion 1/20 Papain:4B8 (w/w) at 30 ˚C for 1 hour in the presence of 5 mM L-cysteine and quenched with 20 mM iodoacetamide. Full-length IgG and Fc regions were removed via protein A chromatography and the flow-through containing 4B8 Fab was concentrated and purified by TSK3000/Superdex200 size exclusion chromatography in 20 mM Hepes pH 7.4, 0.2M NaCl, 5% Glycerol.

Antibody fragments (Fabs) generated by phage display were expressed and purified essentially as described(42) from constructs subcloned into the expression vectors pRH2.2 or pSFV4 (gift from S. Sidhu). DNA was transformed into BL21-Gold(DE3) (Agilent) and used directly to set up 15 mL overnight starter cultures in 2xYT media supplemented with 50 ug/mL ampicillin. Cultures were then inoculated into 1 L of 2xYT media, grown until OD_{600} of ~0.8-1.0, induced with 1 mM IPTG for 4 hours at 37 °C. Cells were harvested by centrifugation and disrupted in lysis buffer containing 20 mM sodium phosphate dibasic pH 7.4, 500 mM NaCl, 1 mM PMSF, and 2 mM DNase, using sonicator (Branson). Lysate was heated to 55 °C for 30 minutes, cleared by centrifugation and incubated with 1 mL of MabSelect ProteinA resin (GE Healthcare) in batch for 1 hour at 4 °C. Resin was washed with 15 column volumes of 20 mM sodium phosphate dibasic pH 7.4, 500 mM NaCl and then eluted with 10 ml 0.1 M acetic acid into tubes containing 1 mL of 1 M Hepes pH 7.5 to immediately neutralize elutions containing Fab fragments. Fabs were then dialyzed against 4 L of 50 mM HEPES pH 7.5 and 200 mM NaCl, concentrated with Millipore concentrators with 30 kDa molecular weight cutoff and stored in aliquots at -80 ˚C. Typical yield from 1 L culture varied depending on Fab fragment and was between 0.5 – 3 mg. For cryo-EM studies Fab CAT06 was modified with H12 elbow variant as described previously(43), resulting in the CAT06/H12 antibody fragment. Briefly, the H12 elbow variant exchanges heavy chain residues (112)SSASTK(117) (numbering according to Kabat (44)) to (112)FNQI-K(117) with one position deleted from the sequence.

Saposin A and Nanodisc Reconstitution

Lipids. All lipids were prepared from thin films. Lipids were dissolved in chloroform, aliquoted into glass vials, dried under nitrogen, and stored at -20 ˚C dry. Unless otherwise noted,

resuspending lipids was accomplished by adding buffer with or without detergent and sonicating 10-30 minutes until clear.

Saposin A nanoparticles. Saposin A nanoparticles containing AtTPC1 were formed by mixing AtTPC1 alone or AtTPC1-Cat06/H12 Fab complexes with soy polar lipids and saposin A in a 1:8:5-10 ratio by mass. A typical preparation consisted of 2.4 mg (8 mg/mL) of NiNTA purified AtTPC1 incubated with 2.4 mg (9 mg/mL) of protein A purified CAT06/H12 (adjusted to 0.05% DDM, 1 mM $CaCl_2$), incubated at room temperature for 5-10 minutes. AtTPC1-Cat06/H12 Fab complexes were then mixed with 4.8 mL of 5 mg/mL soy polar lipids (diluted from a 25 mg/mL stock in 1% DDM) dissolved in Size Exclusion Buffer (20 mM Hepes pH 7.3, 0.2 M NaCl, 5% Glycerol, 1 mM $CaCl_2$, 0.05% DDM) and incubated at room temperature for 30 minutes. Then 9.6 mL (2 mg/mL) saposin A was added, incubated 1 hour at room temperature, then diluted to 40 mL with Size Exclusion Buffer. Detergent was removed by adding 1 g of activated, washed, Bio-Beads SM2 (BIO-RAD) resin overnight at 4˚C. Bio-Beads were activated by incubation in methanol and successively washed with copious amounts of water. The following morning, beads were removed by filtration through 5 µm syringe filter. 0.5 molar equivalent of Fab CAT06/H12 was added, incubated 30 minutes at 4 ˚C, then concentrated to ~0.3 mL in a 100 kDa MWCO concentrator, and filtered prior to injection on a TSK4000 or Superose 6 column equilibrated in Nanodisc Size Exclusion Buffer (20 mM Hepes pH 7.3, 0.2 M NaCl, 1 mM $CaCl_2$). A single fraction was selected for cryo-EM analysis by screening for homogeneous particles by negative-stain EM (Figure S6b-d). Cryo-EM grids were frozen following ultracentrifugation at 100,000x g (TLA-55) for 5 minutes at 4 ˚C without further concentration. AtTPC1-CAT06/H12-saposin A complexes typically eluted from size exclusion at 0.5-1 mg/mL. 16 lipids are observed bound to $AtTPC1_{DDE}$ (Figure S7).

MSP nanodiscs. Reconstitution of AtTPC1 into E3D1 nanodiscs was performed using standard protocols(45). For the purpose of antibody generation by phage display, full-length $AtTPC1_{WT}$ was reconstituted into nanodiscs using biotinylated version of MSP E3D1, and size exclusion fractions corresponding to AtTPC1 in biotinylated nanodiscs were used without the removal of empty nanodiscs. Final mixed lipid-detergent micelles used in reconstitution contained 10 mM soy polar extract, 1 mM CHS, and 30 mM DDM. Nanodisc assembly mix was prepared using purified TPC1, mixed micelles and MSP at 2:10:1000 ratio. All components were mixed together in Nanodisc Size Exclusion Buffer and incubated on ice for 1 hour. Next, 400-500 mg activated Bio-Beads were added per each ml of assembly mix, and the reconstitution reaction was left shaking overnight at 4°C. As a control, empty nanodiscs were prepared using the same phospholipids. All nanodisc samples for phage display experiments were concentrated, supplemented with 5% w/v sucrose, aliquoted, flash-frozen in liquid nitrogen, and kept at -80°C.

Proteoliposomes. Proteoliposomes of full-length wild-type AtTPC1 were formed by resuspending 20mg of soy polar lipids dried from chloroform resuspended in 4 mL Nanodisc Size Exclusion Buffer, subjected to 10x alternating liquid Nitrogen and warm water bath freeze-thaw cycles, then sonicated for 10 min. The opaque mixture was then passed through an Avestin hand extruder with a 400 nm pore size 10x until mildly translucent. Vesicles were disrupted by addition of 69.8 µL 10% DDM added (4 mM final), 12.1 µL 2% CHS in 10% DDM added (0.1 mM final), and 1 mM $CaCl_2$, and stirred 30 minutes at room temperature. 2 mg of AtTPC1 was added to disrupted liposomes (1:10 protein:lipid ratio) and stirred for 1 hour at room temperature using a magnetic “flea” stir bar. To form proteoliposomes, methanol washed Bio-Beads were added in increments of 300 mg, 300 mg, 500 mg, and 1 g in 1-hour intervals at room temperature. The last incubation was done at 4 ˚C overnight. The following morning the samples

were centrifuged at 100,000x g for 1 hour in a table-top ultracentrifuge (TLA-55). The proteoliposome pellet was resuspended in in 0.4 mL of Nanodisc Size Exclusion Buffer. The concentration was estimated by gel and frozen in liquid Nitrogen and stored at -80 ˚C. Empty liposomes were made in a similar fashion by substituting AtTPC1 protein with Size Exclusion Buffer.

Antibody Generation

Hybridoma. Hybridoma cell lines were generated by standard methods at OHSU by Daniel Cawley. Briefly, four Balb/c mice were injected with 25 µg of AtTPC1 proteoliposomes at 0 and 14 days. On day 26, serum was prepared and tested for antibody titer in ELISA. The mice with the highest titers were used to derive hybridomas. The two best responding mice were injected on day 45-55 with 10 µg Ag as a final boost. 4 days later, spleen cells are fused with P3X mouse myeloma cells. Hybridomas were assayed 12 days later in ELISA. All candidate cell lines were expanded and given a secondary ELISA screen 12-14 days later. All antigen specific antibodies were made available as culture supernates for screening. All candidate cell lines are frozen in liquid nitrogen. 14 hybridoma antibodies were identified that specifically bind to immobilized biotinylated AtTPC1 in DDM detergent by ELISA. To select for antibodies that recognize 3D structural epitopes a counter-selection against antibodies that bind linear epitopes on denatured protein in 8M Urea was performed, yielding 5 antibodies that bind only under native conditions by ELISA. Selection of high-affinity antibodies that were capable of complex formation was conducted by fluorescence size exclusion chromatography(46) (FSEC) using FITC-labeled AtTPC1 and hybridoma supernatants containing 10-50 µg/mL whole IgG. FSEC samples were prepared by mixing 1µg FITC-Labeled AtTPC1 with 0.4 mL hybridoma supernatants (supplemented with components to make Size exclusion buffer +0.03 mg/mL Soy Polar Lipids)

694 in a total volume of 490 µL of Size exclusion buffer. Samples were incubated at 25 ˚C for 1 hour
695 or 4 ˚C for 4-5 hours and injected on a Superose 6 column, 0.4 mL/min, equilibrated in Size
696 exclusion buffer at 4 ˚C, using an autosampler and inline fluorescence detector set at
697 excitation=495 nm and emission=518 nm. The fluorescence detector (Shimadzu RF-10AXL)
698 was calibrated before use by injecting varying amounts of FITC-AtTPC1 (0.1 ng-1 µg) with
699 known labelling efficiency.
700 **Phage Display.** To generate Fabs, the efficiency of biotinylation of $AtTPC1_{WT}$-E3D1 nanodiscs
701 was evaluated by pull-down on streptavidin-coated magnetic beads (Promega). Library sorting
702 steps were performed using Fab Library E (DNA kindly provided by S. Koide(47)) based on
703 previous protocols(31, 48). Six independent phage library sorting experiments were performed
704 against biotinylated $AtTPC1_{WT}$ -E3D1 nanodiscs in 2 buffers containing 20 mM Hepes pH 7.3,
705 200 mM NaCl, 5% glycerol, 1% BSA, and either 1 mM $CaCl_2$ or 1 mM EGTA. Additionally, for
706 each $CaCl_2$ or EGTA condition, sorting was carried out in the presence of following ligands:
707 either 1 µM NAADP, 1 µM trans-NED19, or no ligand control to maximize the number of
708 multiple states of TPC1 channel during sorting (Sorting Buffer). Total of five rounds of phage
709 library sorting were performed for each sample with decreasing concentration of immobilized
710 biotinylated TPC1-E3D1 nanodiscs between subsequent rounds in following order 1000 nM, 600
711 nM, 200 nM, 200 nM and 100 nM. Round 1 of sorting was performed manually using nanodisc
712 bound to streptavidin-coated magnetic beads, and upon washing with respective Sorting Buffer,
713 whole beads were used to infect log phase *E. coli* XL-1 strain (Stratagene) in the 2xYT media
714 (Fisher) supplemented with 50 µg/ml ampicillin and 10^9 pfu/ml of KO7 helper phage (NEB)
715 overnight at 37 °C and 280 rpm to amplify the phage particles. The amplified phage particles
716 after round 1 were used as an input for four additional rounds of library sorting performed semi-

automatically with a KingFisher magnetic bead handler (Thermo) according to described protocols(49). Starting from round 2, in every step except elution, the buffer was supplemented with 10-fold molar excess of non-biotinylated empty E3D1 nanodiscs to counter-select for MSP-, lipid-, and non-specific phage particles. Finally, in each of rounds 2-5, phage particles were eluted from magnetic beads by 15-minutes incubation with 1% Fos-Choline-12 in respective Sorting Buffer.

Initial validation of selection clones was performed by single point direct phage ELISA using clones from round 3, 4 and 5. Amplified phage particles at 10-fold dilution were assayed against 50 nM biotinylated nanodiscs (either empty or with AtTPC1) using HRP-conjugated anti-M13 monoclonal antibody (GE Healthcare, #27-9421-01). Assays were performed in respective Sorting Buffer supplemented with 2% BSA. Each Fab clone with A_{450} signal above 0.2 (four times the average background level of the assay) was sequenced; unique Fabs were sub-cloned into pSVF4 or pRH2.2 vectors (kind gift of S. Sidhu), and purified as described above. In total 16 unique Fab sequences were obtained from total of 192 single colonies screened; 9 Fabs from library sorting with $CaCl_2$ and 7 Fabs from library sorting with EGTA.

Cryo-EM Structure Determination

Sample Preparation. Samples were analyzed by negative-stain EM to determine suitability for cryo-EM. To prepare grids, 3 μl of sample at 10–50 μg ml^{-1} was applied to a glow discharged continuous carbon grid, which was then treated with 0.75% (w/v) uranyl formate. Grids were imaged on an FEI Tecnai T12 microscope operated at 120kV at a nominal magnification of 52,000× using an UltraScan 4000 camera (Gatan) or an FEI Tecnai T20 microscope operated at 200kV and at a nominal magnification of 80,000× using a TemCam-F816 8k × 8k CMOS

camera (TVIPS) camera, corresponding to pixel sizes of 2.21 Å and 0.95 Å, respectively, on the specimen.

Grids for cryo-EM were prepared with FEI Mark IV vitrobot. Quantafoil R1.2/1.3 400 mesh holey carbon grids (EMS) were glow-discharged for 30 s. Then 2.5 µl protein sample at a concentration of 0.6-1.5 mg ml^{-1} was applied onto the carbon face of the grids. The grids were blotted with Whatman#1 filter paper for 2-4 s at 100% humidity and plunge frozen in liquid ethane. The grids were loaded onto a 300kV Polara (FEI) with a K2 Summit direct electron detector (Gatan). Data were collected at nominal magnification of 31,000×, corresponding to a physical pixel size of 1.2156 Å (0.6078 Å super resolution pixel size) on the specimen with a dose rate of 7.6 electrons per physical pixel per second. Images were recorded with SerialEM in super-resolution counting mode and a defocus range of −0.8 to −2.0 µm. A total exposure of 12 s was used, with 0.2 s subframes (60 total frames) to give a total dose of 60 electrons per $Å^2$ (1.35 electrons per $Å^2$ per subframe). Data for $AtTPC1_{WT}$ in saposin A was also collected at the Janelia Cryo-EM facility FEI Titan Krios microscope operated at 300kV with a K2 camera with a physical pixel size of 1.02 Å.

Image Processing. For negative-stain data, GCTF(50), Gautomatch (Kai Zhang, url: https://www.mrc-lmb.cam.ac.uk/kzhang/), and RELION-2(51) were used for CTF estimation, particle picking, and 2D classification, respectively. For cryo-EM data, dose-fractionated super-resolution image stacks were drift corrected and binned 2×2 by Fourier cropping using MotionCor2(52) (after discarding the first frame). CTF determination and particle picking was performed on motion-corrected sums without dose-weighting using GCTF and Gautomatch. To generate particle picking templates and initial models a Gaussian reference was used to pick particles and 2D classification was performed in RELION-2 followed by *ab-initio* reconstruction

762 in cryoSPARC. Particles were then picked using six 2D classes as templates. 2D classification,
763 3D classification and refinement procedures were carried out using and RELION-2 and
764 cryoSPARC(53) (Figure S3). After 3D classification the reconstruction was filtered to 30 Å
765 resolution and used as an initial reference model for 3D refinement in cryoSPARC v2 using the
766 beta version of non-uniform refinement yielding a reconstruction with a gold-standard Fourier
767 shell correlation of 3.5 Å with a 0.143 cutoff criterion. The map from cryoSPARC was used for
768 modeling the Fab variable domain. The final 3.3 Å high-resolution reconstruction was performed
769 in RELION-2 using 3D auto-refinement by masking out the saposin A membrane belt and the
770 Fab using a mask created from a 30 Å low-pass filtered model of $AtTPC1_{WT}$. Local resolution
771 estimates were performed using RELION-2. The final maps were sharpened in RELION-2 using
772 a B-factor of -104 and -117 $Å^2$ for the TPC1-Fab-saposin and TPC1-only reconstructions,
773 respectively.

774 State 1 and 2 were identified by focused classification of VSD2 without image alignment
775 using the angles determined from the high-resolution reconstruction (Figure S3). Focused
776 classification benefitted from applying C2 symmetry. After 3D classification each particle set
777 was refined in RELION-2 with global angular searches using a 30Å low pass filtered
778 reconstruction of the combined dataset. The maps for state 1 and 2 extend to 3.7 Å as determined
779 by the gold-standard FSC. These maps were used to build atomic models for VSD2 with local
780 resolution in this region ranging from 4-6 Å as estimated by RELION-2 (Table S1). The final
781 maps were sharpened in RELION-2 using a B-factor of -95 and -86 $Å^2$ for the state and state 2
782 reconstructions, respectively.
783

784 **Structure Determination and Refinement**. The entire structure of $AtTPC1_{DDE}$ excluding VSD2
785 was built into the highest resolution map (High-res; Table S1) manually after initial real-space
786 flexible fitting and refinement of the $AtTPC1_{WT}$ structure into the map using Rosetta (54) with
787 the electron scattering table. Manual fitting in COOT(55), followed by real-space coordinate and
788 B-factor/atomic displacement factor refinement in PHENIX(56) were used in *de novo* building of
789 the NTD, EF-hand, CTD, Ca^{2+}-ions, lipid molecules (palmitic acid and phosphatidic acid), and
790 the Fab-$AtTPC1_{DDE}$ interface. This map was calculated with a mask around TPC1, excluding the
791 Fab. A structure of the Fab-complex (Fab-bound; Table S1) was determined from the same
792 dataset by extending the mask to include the Fab variable domains (V_H and V_L). The Fab was
793 built using a homologous structure of a Fab from the same library (PDB 3PGF) with the variable
794 CDR loops deleted.

795 Building of the state 1 (State 1; Table S1)was accomplished by rigid body alignment of
796 the $AtTPC1_{WT}$ structure to the cryo-EM map using CHIMERA (57) followed by flexible fitting
797 and refinement in Rosetta, and extensive manual fitting in COOT. State 2 (State 2; Table S1) was
798 built by first rotating VSD2 of $AtTPC1_{WT}$ to place S10. Movement of S7-S9 around the S10 axis
799 was done manually in real-space. Gating charges R1-R3 were placed in favored rotamer
800 positions using the rotamer library in COOT and PHENIX, while applying the additional
801 restraint that R1-R3 must contact solvent, a polar side chain, or counter charge in the membrane.
802 One position satisfied these criteria for each gating charge.

803 Model validation employed MolProbity(58) and EMRinger(59). Low resolution maps of
804 $AtTPC1_{WT}$-4B8 were interpreted by flexible fitting of the $AtTPC1_{WT}$ crystal structure and a
805 homology model of 4B8 in real-space using Rosetta. Final $AtTPC1_{DDE}$ coordinates and maps
806 have been deposited in the Electron Microscopy Data Bank (EMDB) under EMDB IDs (High-

807 resolution) 8957, (Fab) 8956, (State 1) 8958, and (State 2) 8960, and the Protein Data Bank
808 (PDB) under PDB IDs 6E1M, 6E1K, 6E1N, and 6E1P.
809
810 **Crystal Structure Determination.** AtTPC1 D376A ($AtTPC1_{DA}$) crystals were obtained in the
811 presence of $CaCl_2$, CHS, soy polar lipids, and 1mM trans-NED19 (NED19), using HiLiDe(60) as
812 described previously(19). Average diffraction was 4 Å, with 10% diffracting to 3.5-3.7 Å
813 resolution, the best being 3.5 Å. Anisotropic resolution was determined using the CCP4 program
814 Truncate(61) and the UCLA Anisotropy Server(62). Crystals were partially dehydrated by
815 incubation with additional 15% (v/v) of polyethylene glycol 300 prior to freezing in liquid
816 nitrogen.
817 X-ray diffraction datasets were collected at the Advanced Light Source (ALS) Beamlines
818 8.3.1 and 5.0.2 and at Stanford Synchrotron Radiation Lightsource (SSRL) Beamline 12-2. Data
819 were reduced using XDS(63). The best native dataset extends to overall resolution 3.5 x 6.0 x 4.5
820 Å (ref.(62)). Phases were calculated by molecular replacement using PHASER(64) and AtTPC1
821 wild-type (PDBID 5DQQ) as a search model. Structure interpretation was using COOT(55), with
822 refinement in PHENIX(56). The structure of $AtTPC1_{DA}$ was refined to 3.5 Å resolution with
823 final R_{work}/R_{free} of 31.84 % and 35.19%. A sharpening B-factor of -142.05 $Å^2$ was used for
824 refinement, as described previously(19). Analysis by Molprobity shows Ramachandran
825 geometries of 93.09%, 6.25%, and 0.66% for favored, allowed, and outliers. The structure
826 contains 11.31% rotamer outliers. For comparison of B-factors between $AtTPC1_{WT}$ (mean
827 Wilson B-factor 108 $Å^2$; PDB ID 5DQQ)(19) and $AtTPC1_{DA}$ (mean Wilson B-factor 109.86 $Å^2$)
828 structures, B-factors were first scaled by adding the difference in mean wilson B-factor (1.86 $Å^2$)
829 to the mean wilson B-factor of the wild-type AtTPC1 crystal structure (PDBID 5DQQ)(19). The

830 $AtTPC1_{DA}$ structure and structure factors have been deposited in the Protein Data Bank (PDB)
831 under PDB ID 6CX0.
832
833 **EPR Spectroscopy**
834 **Sample Preparation for CW-EPR.** Concentrated (7-12 mg/mL) NiNTA-purified $AtTPC1_{cysless}$
835 mutations were incubated with 10-fold molar excess MTSL (MTSL; Toronto Research
836 Chemicals, Inc) dissolved at 10 mg/mL in DMSO for 2 hours at room temperature. The samples
837 were then split in half and treated with either 1mM $CaCl_2$ or 5mM EGTA pH 7.4 prior to
838 filtration and purification by size exclusion chromatography in 1mM $CaCl_2$ or 5mM EGTA pH
839 7.4, respectively. $AtTPC1_{cysless}$ has identical biochemical behavior to $AtTPC1_{WT}$ and maintains
840 structural integrity as evidenced by negative-stain EM analysis. Fractions containing labeled
841 $AtTPC1_{cysless}$ were pooled and concentrated to 5 mg/mL for EPR measurements.
842 **EPR Data Collection.** For continuous wave (CW) EPR experiments, X-band spectra were
843 collected on a Varian E-102 Century series spectrometer fitted with a loop-gap resonator
844 (Medical Advances, Milwaukee, WI). Samples (10 uL) were contained in a 0.64/0.80 mm
845 (i.d./o.d.) quartz capillary (Vitrocom, Mountain Lakes, NJ) and spectra were recorded at room
846 temperature over 100 G with an incident microwave power of 2 mW, modulation amplitude of 1
847 G, and modulation frequency of 100 kHz; typical total scan times were 5 minutes. CW spectra
848 were normalized and corrected for minute deviations in baseline prior to comparison and
849 analysis. All data were plotted using Origin 6 after normalizing the area under integrated CW
850 spectrum.
851 Cryo-EM structural data of $AtTPC1_{DDE}$ has been deposited to the Protein Data Bank under
852 accession codes 6E1K, 6E1M, 6E1N, 6E1P and the Electron Microscopy Data Bank under

accession codes 8956, 8957, 8958, 8960. X-ray structural data of $AtTPC1_{DA}$ has been deposited to the Protein Data Bank under accession code 6CX0. Correspondence and requests for materials should be addressed to R.M.S (stroud@msg.ucsf.edu) and Y.C. (ycheng@ucsf.edu).